Natural Resources Canada | Ressources naturelles Canada

GEOMATICS CANADA
OPEN FILE 37

DInSAR products and applications for the RADARSAT Constellation Mission

S.V. Samsonov, W. Feng, and N. Short

2017

Canada

GEOMATICS CANADA
OPEN FILE 37

DInSAR products and applications for the RADARSAT Constellation Mission

S.V. Samsonov, W. Feng, and N. Short

2017

Permanent link: https://doi.org/10.4095/305958

This publication is available for free download through GEOSCAN (http://geoscan.nrcan.gc.ca/).

Recommended citation
Samsonov, S.V., Feng, W., and Short, N., 2017. DInSAR products and applications for the RADARSAT Constellation Mission; Geomatics Canada, Open File 37, 19 p. https://doi.org/10.4095/305958

Publications in this series have not been edited; they are released as submitted by the author.

Abstract

The Canadian RADARSAT Constellation Mission (RCM) is scheduled for launch in the second half of 2018, to support primarily maritime surveillance (sea ice, surface wind, oil pollution and ship monitoring), disaster management (mitigation, warning, response and recovery), and ecosystem monitoring (agriculture, wetlands, forestry and coastal change). The RCM consists of three C-band Synthetic Aperture Radar (SAR) satellites, equally spaced in a common orbit, providing rapid revisit capability. The RCM offers a selection of beam modes that vary in terms of spatial resolution, coverage, polarization and noise floor. The constellation orbit and beam mode options are sufficient to provide daily imaging opportunities of Canadian territories and Differential Interferometric Synthetic Aperture Radar (DInSAR) acquisitions with four days' revisit time. This new source of SAR data will strengthen operational applications that require a continuous stream of data.

In Canada and around the world, DInSAR is regularly used for detection and monitoring of ground deformation (e.g. uplift, subsidence and horizontal motion). At Natural Resources Canada (NRCan), DInSAR derived information supports diverse activities such as detecting terrain instability in permafrost regions, monitoring glacier and ice cap dynamics, monitoring landslide risk sites, and tracking surface deformation related to bitumen extraction. In partnership with the Canadian Space Agency (CSA), the Canada Centre for Mapping and Earth Observation (CCMEO) at NRCan is developing an automated system for generating standard and advanced deformation products by means of DInSAR from data acquired by RADARSAT-2 and RCM satellites. This processing system consists of software and hardware components and is capable of providing non-expert users with on-demand change detection and deformation products computed from the SAR data. This system will allow scientists and resource managers to efficiently and effectively extract ground displacement information from the thousands of RCM acquisitions collected annually during its mission life.

Table of Contents

List of Figures

List of Tables

1. Introduction

The Canada Centre for Mapping and Earth Observation (CCMEO) is developing an automated system for generating standard and advanced deformation products from Synthetic Aperture Radar (SAR) data acquired by RADARSAT-2 and the upcoming RADARSAT Constellation Mission (RCM) satellites using Differential Interferometric Synthetic Aperture Radar (DInSAR[1]) processing methodology. Background information on DInSAR processing and interpretation can be found in the following publications (in order of relevance) and is briefly summarized in the following sections:

- (Ferretti et al., 2007) part A - guidelines for InSAR processing and interpretation;
- (Bamler and Hartl, 1998; Massonnet and Feigl, 1998; Hooper et al., 2012) – DInSAR review papers;
- (Berardino et al., 2002; Lanari et al., 2004; Samsonov et al., 2011)– SBAS-DInSAR;
- (Strozzi et al., 2007) – offset-tracking;
- (Bechor and Zebker, 2006)– multi-aperture interferometry (MAI);
- (Ferretti et al., 2007) part B – practical approach to InSAR processing;
- (Ferretti et al., 2007) part C – mathematical approach to InSAR processing.

2. Synthetic Aperture Radar

Imaging radar illuminates an area on the ground to create a two-dimensional (2D) image. The radar system generates microwave signals (pulses) that are emitted by the antenna and then measures the portion of the signals reflected back (backscattered) from the area of interest (footprint) using a specialised receiver system (Figure 1). By measuring the time delay between the signal transmission and reception of the backscatter (radar echoes) from different targets, their distance from the radar and thus their locations can be determined. As the radar moves from point A to point B along the satellite flight path, it transmits a pulse at each position obliquely. The return echoes pass through the receiver, and are recorded and a series of signal processing steps permit generation of a radar product of the illuminated area or swath.

[1] Note that InSAR and DInSAR abbreviations are frequently used interchangeably.

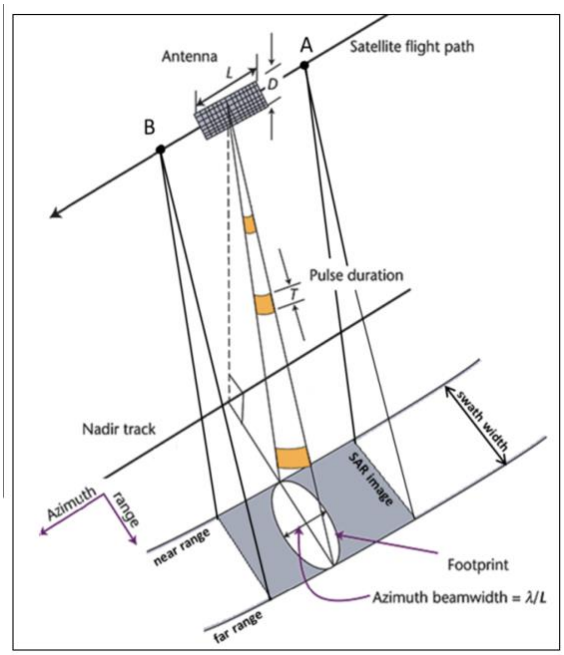

Figure 1: The SAR technique used to synthesize a very long antenna by combining signals (echoes) received by the radar as it moves along its flight track (from point A to point B). A synthetic aperture is constructed by moving a real aperture or antenna through a series of positions along the flight track, edited from (Lubin and Massom, 2007).

In SAR data, range refers to the cross-track dimension perpendicular to the flight direction while azimuth refers to the along-track dimension parallel to the satellite flight direction. The edge of the swath closest to the nadir track is known as the near range while its other edge is known as the far range. Between the near and far range, the radar antenna measures the line-of-sight (LOS) distance between the radar and each target on the surface.

The radar spatial resolution is a function of both the viewing geometry and the microwave signal properties. In addition, the range resolution depends on the duration of the pulse. This means that high range resolution can be achieved by using a shorter pulse length. The azimuthal resolution, known also as the cross-range resolution, depends on the angular width of the transmitted microwave signal and slant range distance. Since radar bandwidth is inversely proportional to the length of the radar antenna, finer azimuthal resolution requires a longer radar antenna. The Synthetic Aperture Radar (SAR) technique is used to synthesize a very long antenna by combining signals (echoes) received by the radar as it moves along its flight track. A synthetic aperture is constructed by moving a real aperture or antenna through a series of positions along a flight track (Houghton, 1989).

Moreover, because the radar moves relative to the ground, the returned echoes are Doppler-shifted: negatively as the radar approaches a target; positively as it moves away. Comparing the Doppler-shifted frequencies to a reference frequency allows many returned signals to be focused on a single point, effectively increasing the length of the antenna that is imaging that particular point. This focusing operation, commonly known as SAR processing, is now done digitally on fast

computer systems. SAR processing algorithms match the variation in Doppler frequency for each point in the image using precise knowledge of the relative motion between the platform and the imaged objects, which is the cause of the Doppler variation in the first place.

2. Differential Interferometric Synthetic Aperture Radar (DInSAR)

DInSAR is a powerful technique for generating ground deformation products by combining two or more SAR acquisitions. The phase of a single SAR acquisition is of no practical use due to its ambiguity. However, the phase difference between two SAR acquisitions, $A_1 = A_0 e^{-i\varphi 1}$ and $A_2 = A_0 e^{-i\varphi 2}$, can be exploited for measuring ground deformation. Here A1 and A2 represent Single Look Complex (SLC) SAR data with amplitude A_0 and phases φ_1 and $\varphi 2$. Two SAR acquisitions can be acquired simultaneously if two SAR antennas are mounted on the same platform (e.g. the Shuttle Radar Topographic Mission), or acquired at different times using repeat orbits of the same satellite (e.g. RADARSAT-2 and RCM). Consecutive radar acquisitions are separated in the time domain, known as temporal baseline and may be separated in the spatial domain, known as spatial (specifically, perpendicular) baseline. Usually the quality of DInSAR products is higher when both temporal and perpendicular baselines are small, but seasonal effects may also affect the quality. Ground deformation is measured along the radar LOS.

The phase difference image or interferogram is the product of one complex SAR image (master) and the complex conjugate of another SAR image (slave) after the slave is co-registered to the master projection with sub-pixel precision. An interferogram is computed with two SAR acquisitions (A_1 and A_2) as following

$$A = A_1 A_2^* = A_0^2 e^{-i(\varphi_1 - \varphi_2)} = A_0^2 e^{i\Delta\varphi} \quad \text{(Eq. 1)}$$

where A_2^* is the complex conjugate of the second SAR image. The phase difference ($\Delta\varphi$) in Eq. 1 can be expressed as

$$\Delta\varphi = \varphi_1 - \varphi_2 = 2\,\frac{2\pi}{\lambda} R - 2\,\frac{2\pi}{\lambda}(R + \delta R) = -\frac{4\pi\delta R}{\lambda} \quad \text{(Eq. 2)}$$

where δR is the slant range change between the two SAR acquisitions and λ is the wavelength of the satellite signal (5.55 cm for RADARSAT-2 and RCM).

In Eq. 2, δR includes various contributions, such as the Earth's curvature ($\Delta\varphi_{flat}$), topography ($\Delta\varphi_{topo}$), deformation ($\Delta\varphi_{def}$), and the sum of other various sources of noise including atmospheric effects ($\Delta\varphi_{noise}$). Therefore, the observed phase difference $\Delta\varphi$ can be expressed as

$$\Delta\varphi = \Delta\varphi_{flat} + \Delta\varphi_{topo} + \Delta\varphi_{def} + \Delta\varphi_{noise} \quad \text{(Eq. 3)}$$

The $\Delta\varphi_{flat}$ component due to the Earth's curvature can be removed using an interferogram flattening process. The $\Delta\varphi_{topo}$ component depends on both ground height and the

perpendicular baseline at the target pixel (Hanssen, 2002), it can be computed using an available Digital Elevation Model (DEM)

$$\Delta\varphi_{\text{topo}} = -\frac{4\pi B_{\perp}}{\lambda R \sin\theta} H_{\text{topo}} \quad \text{(Eq. 4)}$$

where $B_{\perp}$ is the perpendicular baseline, R is the slant range, θ represents the incidence angle and H_{topo} is the topographic height.

The $\Delta\varphi_{\text{noise}}$ component accounts for noise from various sources. One source of phase noise is due to the difference in atmospheric conditions at the time of SAR acquisitions. Atmospheric turbulence causes differences in SAR propagation path lengths. Temporal variability of the atmosphere degrades the precision of interferometric phase that can reach tens of centimeters (Zebker and Villasenor, 1992). Tropospheric phase delay is mostly attributed to the spatial and temporal variability of atmospheric water vapor, resulting in spatial fringes that can also be highly correlated with topography. Moreover, the degree of ionospheric phase delay changes between night and daytime. The ionospheric delay is inversely proportional to the square of the frequency, meaning that shorter wavelengths are less susceptible to the ionospheric effect (Jehle et al., 2010). Existing techniques to correct atmospheric contributions include the incorporation of external data provided by meteorological stations, optical remote sensing products such as MODIS and MERIS (Li et al., 2005, 2006), and statistical analysis (Samsonov et al., 2014).

In order to produce a deformation map, phase filtering to reduce noise and unwrapping are required. Phase unwrapping is the process of adding the correct multiple of 2π to the interferometric fringes to recover the absolute phase difference, since the interferometric phase is wrapped modulo 2π. The process of unwrapping the phase assumes that the deformation pattern is relatively smooth such that the phase differences are less than 2π between two adjacent pixels. This is a critical threshold, which also presents a limitation for DInSAR. Theoretically, the maximum deformation that is measured efficiently with SAR data can be modeled with the wavelength of the radar signals and pixel sizes (e.g. Jiang et al., 2011). For sites with steep deformation gradients one may need to pursue alternative methods, such as offset tracking, to derive reliable deformation measurements from SAR information (Yun et al., 2007).

3. Coherence

The quality of an interferogram, and hence the reliability of derived ground deformation products, is affected by spatial and temporal decorrelation between the two SAR acquisitions (Zebker and Villasenor, 1992; Ferretti et al., 2001). Temporal decorrelation may be caused by ground surface change (e.g. vegetation change, ice or snowmelt, soil moisture change, etc.) and the spatial decorrelation may include Doppler centroid and imaging geometry differences between the two acquisitions. The amount of decorrelation is quantified by estimating

interferometric coherence, which is the cross-correlation of the SAR data pair estimated over a local window

$$\rho = |A| = \frac{\left|A_1 A_2^*\right|}{\sqrt{A_1 A_1^*}\sqrt{A_2 A_2^*}} \quad \text{(Eq. 5)}$$

where ρ is the coherence, which ranges from 0 to 1, with coherence values approaching 1 indicating reliable signals. Therefore, coherence can be used to select areas where the phase information can be used meaningfully. The size of the window is a trade-off between the spatial resolution and an unbiased estimation of the coherence. Small windows ensure high spatial resolution but with likelihood of biased coherence estimation toward higher values (Touzi et al., 1999), whereas large windows may underestimate coherence in heterogeneous surfaces. Coherence products are useful information sources in themselves, providing information about where change has occurred even if that change is not quantifiable.

4. Offset-tracking

Amplitude components of SAR data can be used to measure large local deformation with a subpixel tracking method (e.g. Michel et al., 1999). This approach requires the same repeat pass interferometric SAR data sets as DInSAR and tracks the relative displacement of small image chips by applying a 2-dimensional cross-correlation algorithm to the co-registered SAR image pairs (Gray et al., 2001; Short and Gray, 2004, 2005; Van Wychen et al., 2012). This technique can achieve an accuracy better than 1/20th of the pixel size in the slant range and azimuth directions (Strozzi et al., 2002) but this accuracy is still much less than the accuracy of 1-2 cm provided with DInSAR (Fialko et al., 2001). Since the measurement of a sub-pixel map is scaled within one pixel, the ability of the method can also vary with the real pixel size (Singleton et al., 2014). Therefore, a pair of SAR data with a spatial resolution of 1 m can provide more precise results than a pair of SAR data with a spatial resolution of 30 m. The method has the great advantage of measuring deformation in both azimuth and range directions with a single pair. By combining the 2-dimensional deformation result with a third data source, or making assumptions about local slopes and flow directions, offset-tracking results can be used to derive 3-dimensional deformation measurements.

5. Multiple Aperture Interferometry (MAI)

Multiple Aperture Interferometry (MAI) is another method for detecting large along-track (azimuth) surface displacements (Bechor and Zebker, 2006). Two SAR images, representing master and slave acquisitions, are decomposed into forward and backward SLC data. The MAI method uses forward-looking SLC data to generate a forward looking interferogram, and backward looking SLC data to generate a backward looking interferogram. Complex conjugate multiplication of the forward-looking interferogram by the backward-looking interferogram is then used to generate an MAI interferogram. The MAI result is consistent with the azimuth component derived from offset-tracking. The MAI method produces measurement accuracy of a few centimeters, better than offset-tracking but worse than DInSAR. Note that no DEM data is needed in the MAI processing. Atmospheric noise effects can be largely minimized (Jung et al., 2014), however, good coherent data will be required for successful MAI analysis.

6. Multi-temporal DInSAR

Time series analysis of DInSAR data or multi-temporal DInSAR uses many repeat pass interferograms to monitor ground deformation over an extended period. Persistent Scatterer (PS) methods comprise the first category of multi-temporal DInSAR methods and are based on extracting stable scatterers within SAR images using dispersion methods. The dispersion of a pixel is defined as the ratio of its standard deviation to its mean (also known as coefficient of variation). The PS methods are used in landscapes that present an abundant number of PSs, particularly urban areas. The PS method is not implemented in our system.

The second category of multi-temporal DInSAR includes Small Baseline Subset (SBAS) (Berardino et al., 2002; Lanari et al., 2004; Samsonov et al., 2011), Multidimensional SBAS (MSBAS) (Samsonov and d'Oreye, 2012) and Stanford Method for Persistent Scatterers (StaMPS) (Hooper et al., 2004; Hooper, 2008). These methods are based on the Singular Value Decomposition (SVD) processing of highly coherent interferograms, usually acquired with small temporal and perpendicular baselines. These methods are capable of generating non-linear time-series of ground deformation. The MSBAS method is implemented in our system.

7. Data requirements for InSAR

Conventional DInSAR processing requires two or more single look complex (SLC) products acquired with identical SAR characteristics (wavelength, beam mode and polarization) and virtually identical imaging geometry, essentially limiting DInSAR to repeat pass acquisitions of the same satellite or single track acquisitions from multiple but identical satellites. High resolution and co-polarization (HH or VV) modes are more suitable as they deliver higher interferometric coherence. Orbital maintenance has been a concern in past, because satellite drift can result in pairs with large perpendicular baselines which have lower coherence or may be unsuitable for

interferometry altogether (RADARSAT-1 for example). This however, is becoming less of an issue as the importance of precise orbit maintenance is understood and practiced, as should be the case for RCM.

For performing DInSAR analysis it is important to consider what would be suitable data in terms of resolution and wavelength for the application (Massonnet and Feigl, 1998). Another issue is related to the quality of the DEM used to remove topographic phase contributions from the interferograms. This is particularly critical for mapping spatially small deformation and a high resolution DEM ensures higher accuracy DInSAR products.

8. RADARSAT Constellation Mission

The RCM consists of three C-band (5.55 cm wavelength) satellites orbiting at 586-615 km altitude. The orbit revisit cycle of each individual satellite is twelve days and the orbit revisit cycle of the constellation is four days. The four days DInSAR potential strengthens operational use of SAR data in applications that require continuous collection of data. The RCM data can be acquired in several beam modes with varying spatial resolution, coverage, polarization and noise floor characteristics, as listed in Table 1 and Figure 2. The following polarizations will be available for each beam mode in SLC format:

- Single (HH, HV, VH, VV);
- Dual (HH+HV, VV+VH), HH+VV will be available only for Ship detection, Low noise, and Spotlight beam modes;
- Compact (CP);

The RCM quad-polarization beam mode is considered experimental rather than operational.

- **Table 1: RCM beam modes, where L is the slant range and azimuth spatial sampling, θ is the nominal incidence angle range, R and A are multi-looking numbers in range and azimuth respectively, and NESZ is the nominal Noise Equivalent Sigma Zero that describes the sensitivity of the SAR system.**

Beam Name	Beam type	Resolution (m)	Swath (Km)	Looks (R x A)	L (m)	θ°	NESZ (dB)
Ship Detection	ScanSAR	variable	350	5 x 1	1.4 x 34.4	40 - 58	variable
Low Noise	ScanSAR	100	350	4 x 2	8.7 x 69.1	19 - 58	-25
Low Resolution 100m	ScanSAR	100	500	8 x 1	4.2 x 69.1	19 - 54	-22
Medium Resolution 50m	ScanSAR	50	350	4 x 1	4.2 x 34.5	19 - 58	-22
Medium Resolution 30m	ScanSAR	30	125	2 x 2	4.2 x 23.0	19 - 47	-24
Medium Resolution 16m	Strip-map	16	30	1 x 4	6.3 x 2.2	19 - 47	-25
Quad-Polarization	Strip-map	9	20	1 x 1	3.1 x 2.9	24 - 44	-24
High Resolution 5m	Strip-map	5	30	1 x 1	2.1 x 2.2	19 - 54	-19
Very High Resolution 3m	Strip-map	3	20	1 x 1	1.4 x 1.9	19 - 54	-17
Spotlight	Spotlight	3 x 1	20 x 5	1 x 1	1.4 x 0.5	19 - 47	-17

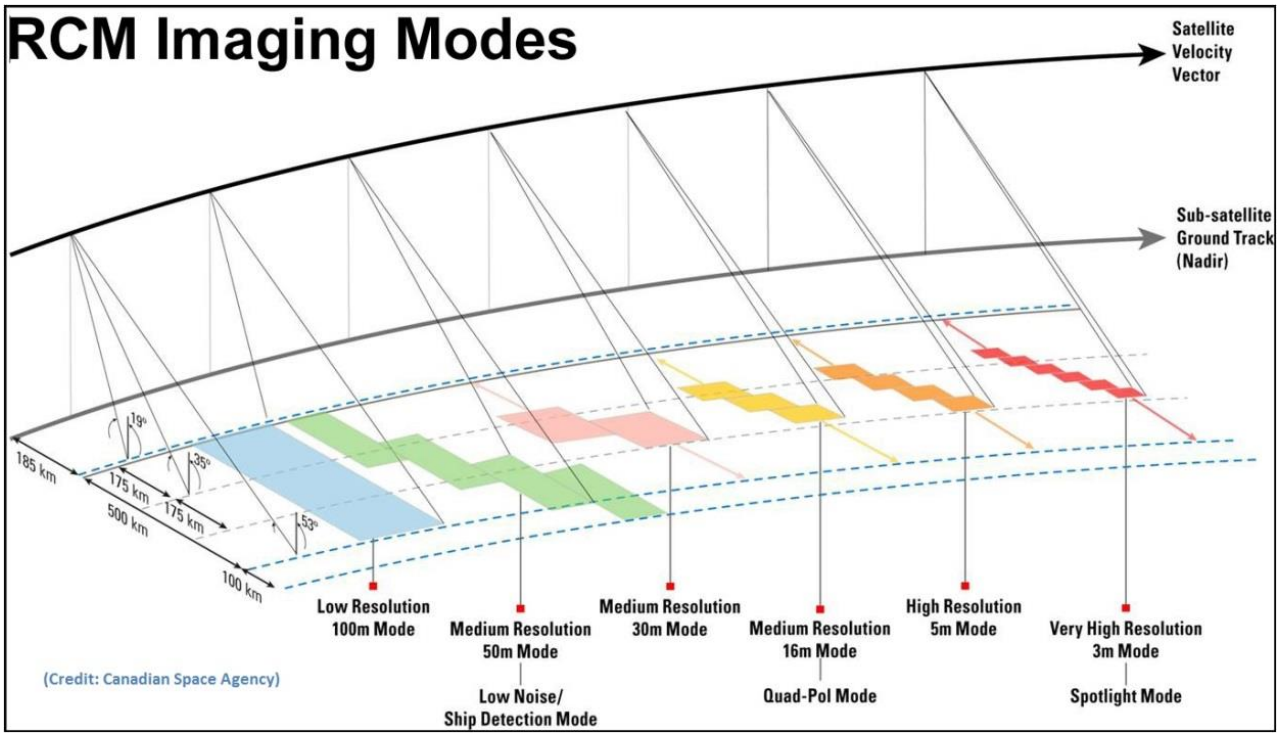

Figure 2: Imaging modes of the RADARSAT Constellation Mission.

9. RCM InSAR Applications

Deformation and change detection products produced with DInSAR can be used in a variety of applications, some of which are listed in Table 2. Each application is characterized by its temporal duration, relative to the RCM orbit revisit cycle of four days, and magnitude of displacement, relative to the RCM wavelength of 5.55 cm. For example, abrupt duration means that events occur almost instantaneously (e.g. earthquake), while gradual duration means that events occur over a period longer than four days (e.g. mining induced subsidence). Small magnitude means displacement smaller than satellite wavelength of 5.55 cm (e.g. inter-seismic motion), while very large magnitude means displacements larger than a few 10s of cm (e.g. earthquake).

Table 2: Supported applications.

Applications	**Duration**	**Displacement Magnitude**
Earthquakes	Abrupt	Small to very large
Volcanoes	Gradual and abrupt	Small to very large
Landslides	Gradual and abrupt	Small to very large
Tectonics	Gradual	Predominantly small
Permafrost	Gradual	Predominantly small
Glacial motion	Gradual	Predominantly very large
Anthropogenic (mining, groundwater, carbon capture and storage-CCS)	Gradual and abrupt	Predominantly small to large
Change detection	Gradual and abrupt	N/A detects coherence loss only

10. RCM InSAR Products

A preliminary list of products is provided in Table 3. When feasible, data will be delivered in GeoTIFF format, in radar coordinates or geocoded.

Table 3: Supported products.

Product	Abbreviation	Description	Format	Unit
Footprint		Image footprint for displaying in Google Earth	kml	
Digital elevation model	DEM	Digital Elevation Model extracted from the source specified through EODMS interface	Float	m
Coregistered SLC images	RSLC	Original SLC images coregistered to master image specified through EODMS interface	Complex	
Coregistered multi-look intensity	RMLI	Coregistered intensity images	Float	dB
Unfiltered coherence	Coherence	Cross-correlation coefficient of the SAR image pair estimated over a small window	Float	
Filtered coherence		Unfiltered coherence after applying adaptive filtering	Float	
Wrapped unfiltered phase		Differential interferogram of the SAR image pair, flattened and topographic phase removed	Float	rad
Wrapped filtered phase		Differential interferogram after applying adaptive filtering	Float	rad
Unwrapped filtered phase		Unwrapped filtered differential interferogram	Float	rad
Displacement	DInSAR	Ground displacement along the satellite line of sight (LOS)	Float	cm
Multi-temporal displacements	SBAS-DInSAR	Time series of ground displacements for each SLC epoch	Float	cm
Offset-tracking	Offset-tracking	Range and azimuth offset maps	Float	m
Multi-aperture interferometry	MAI	MAI differential interferogram	Float	m

11. RCM InSAR Applications and Recommended Products

The following Table 4 lists recommended products for each application.

Table 4: Applications and recommended products.

Applications/Recommended Products	DInSAR	SBAS-DInSAR	Offset-tracking	MAI	RSLC	RMLI	Coherence
Earthquakes (co-seismic)	☑		☑	☑			
Volcanoes	☑	☑					
Landslides	☑	☑					
Tectonics	☑	☑					
Permafrost		☑					
Glacial motion	☑		☑	☑			
Anthropogenic (mining, groundwater, CCS)	☑	☑					
Change detection					☑	☑	☑

12. RCM InSAR System and User Access

To generate DInSAR products using the automated DInSAR processing system, a user needs to access the Earth Observations Data Management Systems (EODMS) interface to choose input data and specific processing parameters. The processing request is translated into an xml file and transferred, along with the SAR data and appropriate DEM segment, to the High Performance Computer in Dorval (HPC Dorval) where the DInSAR processing system is hosted, and placed in the Inbox.

Once the DInSAR processing is completed, results are picked up from the Outbox (transfer is initiated by EODMS) and transferred back to EODMS where they can be accessed by the user. The interactions between EODMS and the automated DInSAR processing system are performed using *ssh* protocol. It is expected that the automated DInSAR processing system can handle up to five orders per day with a maximum capacity of 50GB per order. The life cycle is set to seven days with a total capacity of around 2TB. The processing system is based on the commercial Gamma Remote Sensing processing software and an ensemble of automatization scripts using *bash*, *Python* and *C*. The interface of EODMS has several tabs to facilitate the building of a processing request by the user. Registration is required for using the EODMS system.

13. Acknowledgement

The authors would like to thank Dr. K. Omari for contributing to the first version of this document.

14. References

Bamler, R., and P. Hartl, 1998, Synthetic aperture radar interferometry Synthetic aperture radar interferometry: Inverse Problems, v. 14, no. 4, p. 55, doi:10.1088/0266-5611/14/4/001.

Bechor, N. B. D., and H. A. Zebker, 2006, Measuring two-dimensional movements using a single InSAR pair: Geophysical Research Letters, v. 33, no. 16, doi:10.1029/2006GL026883.

Berardino, R. P., G. Fornaro, R. Lanari, and E. Sansosti, 2002, new algorithm for surface deformation monitoring based on small baseline differential interferograms: IEEE Transactions on Geoscience and Remote Sensing, v. 40, no. 11, p. 23375–2383.

Data, S. S. A. R., M. Jehle, S. Member, O. Frey, D. Small, and E. Meier, 2010, Measurement of Ionospheric TEC in: IEEE Transactions on Geoscience and Remote Sensing, v. 48, no. 6, p. 2460–2468.

Ferretti, A., A. Monti-guarnieri, C. Prati, and F. Rocca, 2007, InSAR Principles: Guidelines for SAR Interferometry Processing and Interpretation (TM-19, February 2007): 71 p.

Ferretti, A., C. Prati, and F. Rocca, 2001, Permanent scatterers in SAR interferometry: IEEE Transactions on Geoscience and Remote Sensing, v. 39, no. 1, p. 8–20, doi:10.1109/36.898661.

Fialko, Y., M. Simons, and D. Agnew, 2001, The complete (3-D) surface displacement field in the epicentral area of the 1999 Mw 7.1 Hector Mine earthquake, California, from space geodetic observations: Geophysical Research Letters, v. 28, no. 16, p. 3063–3066, doi:10.1029/2001GL013174.

Gray, A. L., N. Short, K. E. Mattar, and K. C. Jezek, 2001, Velocities and Flux of the Filchner Ice Shelf and its Tributaries Determined from Speckle Tracking Interferometry: Canadian Journal of Remote Sensing, v. 27, no. 3, p. 193–206, doi:10.1080/07038992.2001.10854936.

Hanssen, R. F., 2002, RADAR Interferomotry: Data Interpretation and Error Analysis.

Hooper, A. J., 2008, A combined multi-temporal InSAR method incorporating persistent scatterer and small baseline approaches: Geophysical Research Letters, v. 35, no. 16, doi:10.1029/2008GL034654.

Hooper, A., D. Bekaert, K. Spaans, and M. Arikan, 2012, Recent advances in SAR interferometry time series analysis for measuring crustal deformation: Tectonophysics, v. 514–517, p. 1–13, doi:10.1016/j.tecto.2011.10.013.

Hooper, A., H. Zebker, P. Segall, and B. Kampes, 2004, A new method for measuring deformation on volcanoes and other natural terrains using InSAR persistent scatterers: Geophysical Research Letters, v. 31, no. 23, p. 1–5, doi:10.1029/2004GL021737.

Houghton, J. T., 1989, Introduction to the physics and techniques of remote sensing: Physics of the Earth and Planetary Interiors, v. 54, no. 1–2, p. 194, doi:10.1016/0031-9201(89)90201-X.

Jiang, M., Z. W. Li, X. L. Ding, J. J. Zhu, and G. C. Feng, 2011, Modeling minimum and maximum detectable deformation gradients of interferometric SAR measurements: International Journal of Applied Earth Observation and Geoinformation, v. 13, no. 5, p. 766–777, doi:10.1016/j.jag.2011.05.007.

Jung, H.-S., W.-J. Lee, and L. Zhang, 2014, Theoretical accuracy of along-track displacement measurements from multiple-aperture interferometry (MAI): Sensors (Switzerland), v. 14, no. 9, p.

17703–17724, doi:10.3390/s140917703.

Lanari, R., O. Mora, M. Manunta, J. J. Mallorqui, P. Berardino, and E. Sansosti, 2004, A small-baseline approach for investigating deformations on full-resolution differential SAR interferograms: IEEE Transactions on Geoscience and Remote Sensing, v. 42, no. 7, p. 1377–1386, doi:10.1109/TGRS.2004.828196.

Li, Z., E. J. Fielding, P. Cross, and J.-P. Muller, 2006, Interferometric synthetic aperture radar atmospheric correction: GPS topography-dependent turbulence model: Journal of Geophysical Research: Solid Earth, v. 111, no. 2, doi:10.1029/2005JB003711.

Li, Z., J.-P. Muller, P. Cross, and E. J. Fielding, 2005, Interferometric synthetic aperture radar (InSAR) atmospheric correction: GPS, Moderate Resolution Imaging Spectroradiometer (MODIS), and InSAR integration: Journal of Geophysical Research B: Solid Earth, v. 110, no. 3, p. 1–10, doi:10.1029/2004JB003446.

Lubin, D., and R. Massom, 2007, Remote sensing of earth's polar regions: Opportunities for computational science: p. 58–71, doi:10.1109/MCSE.2007.16.

Massonnet, D., and K. L. Feigl, 1998, Radar interferometry and its application to changes in the Earth's surface: Reviews of Geophysics, v. 36, no. 4, p. 441–500, doi:10.1029/97RG03139.

Michel, R., and J.-P. Avouac, 1999, Measuring near field coseismic displacement from SAR images: application to the Landers earthquake: p. 3017–3020.

Samsonov, S., and N. d'Oreye, 2012, Multidimensional time-series analysis of ground deformation from multiple InSAR data sets applied to Virunga Volcanic Province: Geophysical Journal International, v. 191, no. 3, p. 1095–1108, doi:10.1111/j.1365-246X.2012.05669.x.

Samsonov, S., M. van der Kooij, and K. Tiampo, 2011, A simultaneous inversion for deformation rates and topographic errors of DInSAR data utilizing linear least square inversion technique: Computers and Geosciences, v. 37, no. 8, p. 1083–1091, doi:10.1016/j.cageo.2011.01.007.

Samsonov, S. V., A. P. Trishchenko, K. Tiampo, P. J. González, Y. Zhang, and J. Fernández, 2014, Removal of systematic seasonal atmospheric signal from interferometric synthetic aperture radar ground deformation time series: Geophysical Research Letters, v. 41, no. 17, p. 6123–6130, doi:10.1002/2014GL061307.

Short, N. H., and A. L. Gray, 2005, Glacier dynamics in the Canadian High Arctic from RADARSAT-1 speckle tracking: Canadian Journal of Remote Sensing, v. 31, no. 3, p. 225–239, doi:10.5589/m05-010.

Short, N. H., and A. L. Gray, 2004, Potential for RADARSAT-2 interferometry: Glacier monitoring using speckle tracking: Canadian Journal of Remote Sensing, v. 30, no. 3, p. 504–509, doi:10.5589/m03-071.

Singleton, A., Z. Li, T. Hoey, and J.-P. Muller, 2014, Evaluating sub-pixel offset techniques as an alternative to D-InSAR for monitoring episodic landslide movements in vegetated terrain: Remote Sensing of Environment, v. 147, p. 133–144, doi:10.1016/j.rse.2014.03.003.

Strozzi, T., A. Luckman, T. Murray, U. Wegmuller, and C. L. Werner, 2002, Glacier motion estimation using SAR offset-tracking procedures: IEEE Transactions on Geoscience and Remote Sensing, v. 40, no. 11, p. 2384–2391, doi:10.1109/TGRS.2002.805079.

Strozzi, T., U. Wegmüller, C. Werner, A. Wiesmann, and M. Santoro, 2007, Potential of a C-band SAR mission with 12-day repeat cycle to derive ice surface velocity with interferometry and offset

tracking, *in* International Geoscience and Remote Sensing Symposium (IGARSS): p. 4229–4232, doi:10.1109/IGARSS.2007.4423784.

Touzi, R., A. Lopes, J. Bruniquel, and P. W. Vachon, 1999, Coherence estimation for SAR imagery: IEEE Transactions on Geoscience and Remote Sensing, v. 37, no. 1 PART 1, p. 135–149, doi:10.1109/36.739146.

Van Wychen, W., L. Copland, L. Gray, D. Burgess, B. Danielson, and M. Sharp, 2012, Spatial and temporal variation of ice motion and ice flux from Devon Ice Cap, Nunavut, Canada: Journal of Glaciology, v. 58, no. 210, p. 657–664, doi:10.3189/2012JoG11J164.

Yun, S.-H., H. Zebker, P. Segall, A. Hooper, and M. Poland, 2007, Interferogram formation in the presence of complex and large deformation: Geophysical Research Letters, v. 34, no. 12, doi:10.1029/2007GL029745.

Zebker, H. A., and J. Villasenor, 1992, Decorrelation in Inteferometric Radar Echoes: IEEE Transactions on Geoscience and Remote Sensing, v. 30, no. 5, p. 950–959.